

# Facile Integration between Si and Catalyst for High-Performance Photoanodes by a Multifunctional Bridging Layer

Beidou Guo,<sup>‡,§</sup> Aisha Batool,<sup>‡,§</sup> Guancai Xie,<sup>‡,§</sup> Rajender Boddula,<sup>‡</sup> Liangqiu Tian,<sup>‡,§</sup> Saad Ullah Jan,<sup>‡,§</sup> and Jian Ru Gong<sup>\*,‡,§</sup>

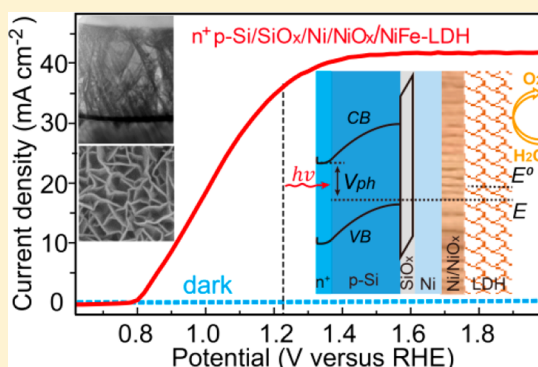
<sup>‡</sup>Chinese Academy of Sciences (CAS) Key Laboratory of Nanosystem and Hierarchy Fabrication, CAS Center for Excellence in Nanoscience, National Center for Nanoscience and Technology, Beijing 100190, People's Republic of China

<sup>§</sup>University of CAS, Beijing 100049, People's Republic of China

## Supporting Information

**ABSTRACT:** Designing high-quality interfaces is crucial for high-performance photoelectrochemical (PEC) water-splitting devices. Here, we demonstrate a facile integration between polycrystalline n<sup>+</sup>p-Si and NiFe-layered double hydroxide (LDH) nanosheet array by a partially activated Ni (Ni/NiO<sub>x</sub>) bridging layer for the excellent PEC water oxidation. In this model system, the thermally deposited Ni interlayer protects Si against corrosion and makes good contact with Si, and NiO<sub>x</sub> has a high capacity of hole accumulation and strong bonding with the electrodeposited NiFe-LDH due to the similarity in material composition and structure, facilitating transfer of accumulated holes to the catalyst. In addition, the back illumination configuration makes NiFe-LDH sufficiently thick for more catalytically active sites without compromising Si light absorption. This earth-abundant multicomponent photoanode affords the PEC performance with an onset potential of ~0.78 V versus reversible hydrogen electrode (RHE), a photocurrent density of ~37 mA cm<sup>-2</sup> at 1.23 V versus RHE, and retains good stability in 1.0 M KOH, the highest water oxidation activity so far reported for the crystalline Si-based photoanodes. This bridging layer strategy is efficient and simple to smooth charge transfer and make robust contact at the semiconductor/electrocatalyst interface in the solar water-splitting systems.

**KEYWORDS:** Water oxidation, Si-based photoanode, NiFe-layered double hydroxide, transition metal catalyst, interfacial engineering, device integration



The promising conversion of intermittent solar radiation into a storable, clean, and sustainable hydrogen fuel through photoelectrochemical (PEC) water splitting demands efficient, stable, and cost-effective materials.<sup>1–3</sup> Over four decades of pursuit, no single material has been found to meet all these requirements, so developing multicomponent systems that integrate high-efficiency photoabsorbers with high-turnover catalysts is attracting more attention.<sup>4–8</sup> Earth-abundant Si, which is widely used in the electronics and photovoltaic industries, has a suitable bandgap (1.1 eV) for absorbing a larger portion of the solar spectrum, superior charge transport properties comparing to metal oxide semiconductors, and mature fabrication technology for device integration, generally leading to higher efficiencies as an attractive photoabsorber.<sup>9–15</sup> Unfortunately, the stability of Si in aqueous solution is poor,<sup>16,17</sup> especially prone to corrosion in the photoanode, where the sluggish oxygen evolution reaction (OER) is the bottleneck of water splitting.<sup>18</sup> Integration of catalysts with Si often improves the PEC device performance by expediting OER<sup>18–34</sup> and/or protects Si against corrosion.<sup>19–27</sup> So far, most studies have been focused on engineering interfacial energetics for higher photovoltage in Si-based PEC devices,

such as suppressing surface charge recombination by inserting an insulator layer as in the metal–insulator–semiconductor (MIS) architecture which is common for Si-based photoelectrodes,<sup>18,19,21–23</sup> tuning the band structure energetics.<sup>19–22,29–32,34–36</sup> However, there is always a trade-off between light shielding and catalytic performance, so the transparent property of the catalyst is required.<sup>21</sup> Otherwise, the high-cost noble-metal catalysts or expensive film coating facilities<sup>22,33</sup> often used are unrealistic for future large-scale water-splitting applications.<sup>20,29</sup>

Recently, transition metal compounds with high OER catalytic activity in the alkaline electrolytes, high abundance, eco-friendly property, and facile preparation have appeared to be a family of potential catalysts.<sup>8,37</sup> Especially for the high-efficient NiFe-layered double hydroxide (LDH), its unique layered structure is favorable for diffusion of water molecules and fast release of gaseous products.<sup>38,39</sup> However, LDH is

**Received:** December 18, 2017

**Revised:** January 19, 2018

**Published:** January 23, 2018

difficult to directly incorporate into the MIS architecture,<sup>18,23</sup> and the open-channel architecture cannot well protect Si from electrolyte corrosion.<sup>38</sup> Herein, we demonstrate a facile integration between the attractive photoabsorber Si and the high-turnover NiFe-LDH nanosheet array by a partially activated Ni bridging layer for the excellent PEC water oxidation performance. The designed n<sup>+</sup>p-Si/SiO<sub>x</sub>/Ni/NiO<sub>x</sub>/NiFe-LDH model system has a few key features: (1) the Ni metal layer is used to protect Si against corrosion because the Ni-based anodes have long been used in industrial water electrolysis with excellent stability;<sup>40</sup> (2) Ni is an attractive interface for buried junction-PEC architectures owing to its ability to make excellent contact with Si and is easily deposited by a variety of techniques (thermal deposition in our case);<sup>35,41</sup> (3) NiO<sub>x</sub> has a high capacity of hole accumulation and strong bonding with the electrodeposited NiFe-LDH due to the similarity in material composition and structure, facilitating transfer of accumulated holes to the catalyst; and (4) this anode structure allows back illumination from the Si substrate, so NiFe-LDH can be sufficiently thick for more catalytically active sites without concerns about any light shielding issues.<sup>10</sup> This earth-abundant multicomponent photoanode affords excellent PEC performance with a very low onset potential ( $\sim 0.78$  V versus reversible hydrogen electrode, RHE), a high photocurrent density ( $\sim 37$  mA cm<sup>-2</sup> at 1.23 V versus RHE), the maximum solar-to-oxygen conversion efficiency ( $\sim 4.3\%$  at 1.02 V versus RHE) and retains the activity for 68 h in 1.0 M KOH under simulated AM 1.5G irradiation at 1 sun. To the best of our knowledge, it is the highest OER activity so far reported for the crystalline Si-based photoanodes (Table S1, Supporting Information). Furthermore, the underlying mechanism for interfacial engineering is systematically analyzed.

The schematic illustration of integrating NiFe-LDH onto the polycrystalline n<sup>+</sup>p-Si substrate through a partially activated Ni interlayer is shown in Figure 1. First, the Ni metal film was

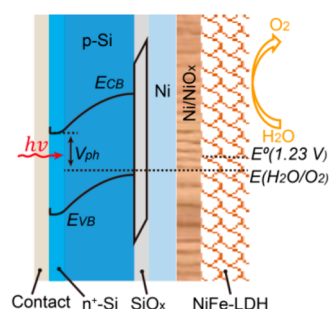


**Figure 1.** Cross-sectional schematic and energy band alignment of the designed multicomponent n<sup>+</sup>p-Si/SiO<sub>x</sub>/Ni/NiO<sub>x</sub>/NiFe-LDH photoanode for water oxidation.

thermally deposited on the p-side surface of n<sup>+</sup>p-Si with native SiO<sub>x</sub>. Then, this Ni film was partially activated in a PEC three-electrode system to form a thin NiO<sub>x</sub> layer on its surface. Finally, the NiFe-LDH nanosheet array was electrodeposited onto the NiO<sub>x</sub> surface (see experimental and characterization details in Figures S1–S4, Supporting Information).

The structure and morphology characterizations of the designed photoanode are shown in Figure 2. Figure 2a displays the cross-sectional transmission electron microscopy (TEM) image of the n<sup>+</sup>p-Si/SiO<sub>x</sub>/Ni/NiO<sub>x</sub>/NiFe-LDH photoanode with a porous NiFe-LDH layer. A thin native SiO<sub>x</sub> layer is observable at the interface between Si and Ni (Figure 2b),

which is also corroborated by the Auger electron spectroscopy depth profiling (Figure S3a, Supporting Information). The amorphous NiO<sub>x</sub> layer encasing the Ni particles, which has intimate contact with the NiFe-LDH overlayer, is formed on the Ni film (Figure 2c, Figure S3b,c, Supporting Information). The top-view and side-view scanning electron microscopy (SEM, Figure 2d, Figure S3d in Supporting Information) and the digital (Figure S3e, Supporting Information) images disclose the microscopic nanosheet array structure and the macroscopic homogeneous flat film of NiFe-LDH with the thickness varying from  $\sim 1$  to  $3$   $\mu$ m on the surface of the textured Si substrate. The high-resolution TEM image (Figure 2e) reveals the fringe spacing of  $0.26$  nm which agrees well with the NiFe-LDH spacing of the (012) lattice plane in the XRD pattern (Figure S3f, Supporting Information), further confirming the formation of NiFe-LDH on the surface of the photoanode. The PEC performance of the n<sup>+</sup>p-Si/SiO<sub>x</sub>/Ni/NiO<sub>x</sub>/NiFe-LDH photoanode was evaluated in a three-electrode voltammetry configuration in  $1.0$  M KOH solution under simulated AM 1.5G back illumination at 1 sun without correction for resistance losses. The optimized photoanode affords a typical photocurrent onset potential ( $V_{on}$ , defined as the potential required to achieve an anodic current of  $0.1$  mA cm<sup>-2</sup>)<sup>29</sup> of  $\sim 0.78$  V versus RHE, a current density of  $\sim 37$  mA cm<sup>-2</sup> at  $1.23$  V ( $E^0(\text{O}_2/\text{H}_2\text{O})$ , the equilibrium potential for water oxidation at pH = 13.6) versus RHE, and a saturation current density of  $\sim 41$  mA cm<sup>-2</sup> (red solid curve in Figure 3), which is the 93.8% of the theoretical value ( $43.7$  mA cm<sup>-2</sup>) that crystalline Si can afford.<sup>30,42</sup> The dark current is near zero (green dashed curve in Figure 3), implying that the observed current under illumination is related to the photogenerated charge carriers. These results of our designed photoanode show the best performance so far comparing to any n-Si or np<sup>+</sup>-Si based photoanodes integrated with noble metal or earth-abundant catalyst.<sup>24</sup> To ensure the reproducibility of the results, over 20 samples with the same configuration were tested, and the n<sup>+</sup>p-Si/SiO<sub>x</sub>/Ni/NiO<sub>x</sub>/NiFe-LDH photoanode yielded photocurrent onset potentials of  $0.78 \pm 0.02$  V versus RHE, and the highest photocurrent density of  $\sim 37 \pm 2$  mA cm<sup>-2</sup> at  $1.23$  V versus RHE.

By comparing the theoretical O<sub>2</sub> production calculated from the photocurrent to the actual O<sub>2</sub> yield, the average Faradaic efficiency was obtained, which is  $\sim 100\%$ , indicating the efficient splitting of water during the PEC water oxidation reaction (Figure S5a, Supporting Information). And considering the 100% Faradaic efficiency, the applied bias photon-to-current efficiency (ABPE, also called the ideal solar-to-O<sub>2</sub> conversion efficiency) of this photoelectrode is  $4.3\% \pm 0.2\%$  at  $1.02$  V versus RHE (Figure S5b, Supporting Information). Stability is another important feature to estimate the application potential of the fabricated photoanode. The PEC stability of this n<sup>+</sup>p-Si/SiO<sub>x</sub>/Ni/NiO<sub>x</sub>/NiFe-LDH photoanode is found to maintain a photocurrent density of  $\sim 9$  mA cm<sup>-2</sup> for 68 h of continuous operation in  $1.0$  M KOH solution as evaluated by chronoamperometric response (Figure S5c, Supporting Information). The variation of the current density was caused by the absorption/desorption of O<sub>2</sub> bubbles and fluctuations in the illuminated light intensity. After the stability test, the morphology of NiFe-LDH shows a negligible change (Figure S5d, Supporting Information), and the textured polycrystalline Si substrate basically keeps intact (Figure S6, Supporting Information). Although a small amount of nanoscale etch pits appear, nearly all its PEC activity was able to retain for some

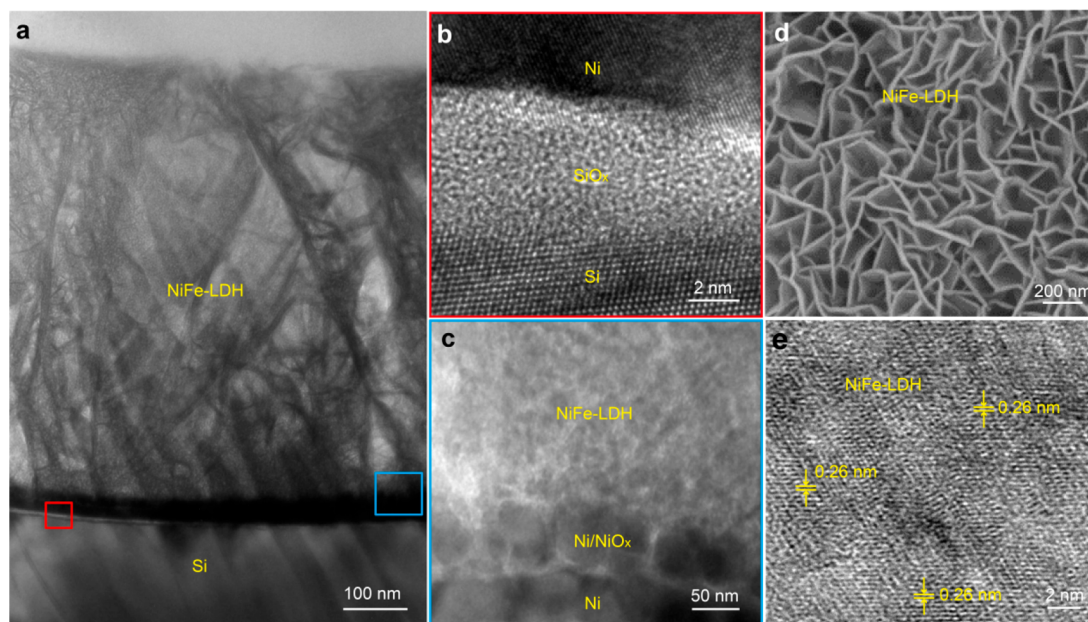


**Figure 2.** Structure and morphology characterizations of the designed photoanode. (a) Cross-sectional TEM image of the  $n^+p$ -Si/SiO<sub>x</sub>/Ni/NiO<sub>x</sub>/NiFe-LDH photoelectrode. High-resolution TEM images of (b) Si/SiO<sub>x</sub>/Ni structure and (c) a particle-like Ni/NiO<sub>x</sub> layer between the Ni metal layer and the NiFe-LDH overlayer, enlarged from the rectangular areas outlined in (a) corresponding to their respective border color. (d) Top-view SEM and (e) high-resolution TEM images of NiFe-LDH.

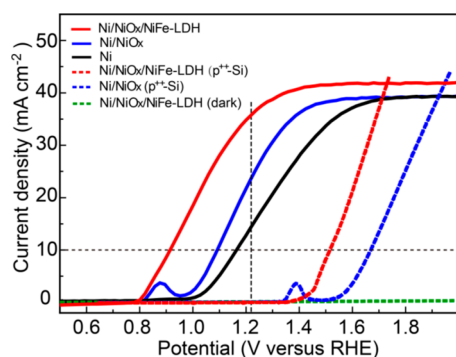


**Figure 3.** PEC performance of photoanodes.  $J$ - $V$  behavior of Ni/NiO<sub>x</sub>/NiFe-LDH (under illumination, red solid curve; in the dark, green dashed curve), Ni/NiO<sub>x</sub> (blue solid curve), Ni (black solid curve) coated  $n^+p$ -Si/SiO<sub>x</sub> anodes, and Ni/NiO<sub>x</sub>/NiFe-LDH (red dashed curve) and Ni/NiO<sub>x</sub> (blue dashed curve) coated non-photoactive  $p^{++}$ -Si electrodes (here the degenerate  $p^{++}$ -Si simply acts as a conductive substrate). The vertical and horizontal black dashed lines are for the convenience of comparison of the water oxidation activity of all electrodes at the equilibrium potential for water oxidation and the potential needed to reach the current density of 10 mA cm<sup>-2</sup>.

time in the next round of the stability test as previously reported.<sup>21</sup>

To explore the underlying mechanism for the excellent PEC performance of the  $n^+p$ -Si/SiO<sub>x</sub>/Ni/NiO<sub>x</sub>/NiFe-LDH photoanode, we investigated the respective role of the different deposition layers. The bare  $n^+p$ -Si anode displays a very low photocurrent density (<1 mA cm<sup>-2</sup>) and its performance decays rapidly within three successive cyclic voltammetry (CV) sweeps (Figure S7, Supporting Information). After depositing the 30 nm Ni film, the initial  $J$ - $V$  curve of  $n^+p$ -Si/SiO<sub>x</sub>/Ni with the photocurrent onset potential ( $V_{on}$ ) of  $\sim$ 1.0 V versus RHE and the current density of  $\sim$ 14.2 mA cm<sup>-2</sup> at 1.23 V versus RHE (black solid curve in Figure 3) indicates that Si corrosion is

greatly inhibited because of the Ni film protection. After activation, the PEC activity of the anode shows improved performance with  $V_{on}$  of  $\sim$ 0.965 V and a current density of  $\sim$ 23.6 mA cm<sup>-2</sup> at 1.23 V versus RHE (blue solid curve in Figure 3). The Ni metal oxidation process on the anode was investigated by X-ray photoelectron spectroscopy (XPS). The Ni 2p peaks display that the signal of metallic Ni for  $n^+p$ -Si/SiO<sub>x</sub>/Ni almost disappears and the Ni<sup>2+</sup> and Ni<sup>3+</sup> signals become dominant (black and blue curves in Figure 4). During

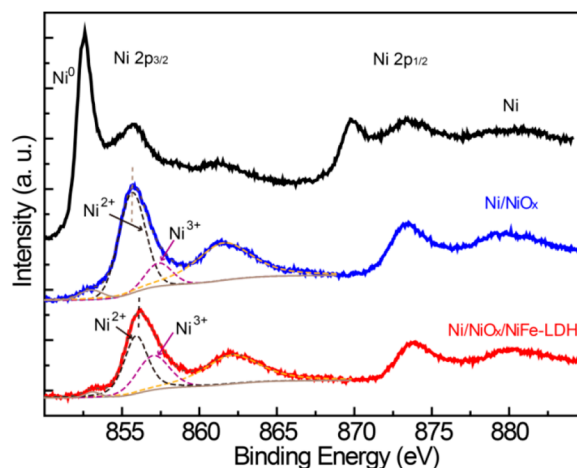


**Figure 4.** Ni 2p XPS spectra of Ni, Ni/NiO<sub>x</sub>, and Ni/NiO<sub>x</sub>/NiFe-LDH coated  $n^+p$ -Si/SiO<sub>x</sub> photoanodes.

the OER, the Ni<sup>2+</sup> resting state in Ni(OH)<sub>2</sub> is oxidized to Ni<sup>3+</sup> in NiOOH, which reacts with OH<sup>-</sup> to evolve O<sub>2</sub> as active sites.<sup>25,33,43</sup> Because of the main contribution of the  $n^+p$ -Si junction,<sup>31</sup> the generated photovoltage ( $V_{ph}$ ) of the  $n^+p$ -Si/SiO<sub>x</sub>/Ni/NiO<sub>x</sub> photoanode is  $\sim$ 578 mV as manifested by the potential difference between  $n^+p$ -Si/SiO<sub>x</sub>/Ni/NiO<sub>x</sub> under illumination (blue solid curve in Figure 3) and a metallic



(heavily doped)  $p^{++}$ -Si (0.001 to 0.005  $\Omega$  cm) coated with Ni/NiO<sub>x</sub> in the dark (blue dashed curve in Figure 3) at 10 mA cm<sup>-2</sup> (see Supporting Information for the detailed explanation),<sup>19,21,29,34</sup> which is the approximate operational current density expected for overall solar-to-fuel conversion devices achieving 10% efficiency and is also a critical figure of merit for OER catalysts.<sup>44</sup>

After NiFe-LDH deposition,  $V_{on}$  in  $n^+p$ -Si/SiO<sub>x</sub>/Ni/NiO<sub>x</sub>/NiFe-LDH shows a further negative shift of  $\sim 180$  mV relative to that of  $n^+p$ -Si/SiO<sub>x</sub>/Ni/NiO<sub>x</sub>, which is equal to the cathodic shift of the potential required to oxidize water at the current density of 10 mA cm<sup>-2</sup> between the two electrodes (Figure 3). The  $V_{ph}$  of  $\sim 608$  mV is generated in  $n^+p$ -Si/SiO<sub>x</sub>/Ni/NiO<sub>x</sub>/NiFe-LDH as measured by the potential difference between this illuminated photoanode and  $p^{++}$ -Si/SiO<sub>x</sub>/Ni/NiO<sub>x</sub>/NiFe-LDH electrode in the dark. The negative shift ( $\sim 35$  mV) of the flatband voltage ( $V_{fb}$ ) in the Mott–Schottky (MS) plot of  $n^+p$ -Si/SiO<sub>x</sub>/Ni/NiO<sub>x</sub>/NiFe-LDH relative to that of  $n^+p$ -Si/SiO<sub>x</sub>/Ni/NiO<sub>x</sub> (Figure S8a, Supporting Information) implies that deposition of NiFe-LDH induces a larger upward band-bending at the surface of Si, which causes an increase of  $\sim 30$  mV in  $V_{ph}$  and also promotes the charge separation and the motion of holes toward the OER catalyst/electrolyte interface.<sup>21</sup>  $V_{ph}$  and OER kinetic overpotential ( $\eta_k$ ) are the two important factors in influencing  $V_{on}$ , which is described by (see details in the Supporting Information)

$$V_{on} = \eta_k - V_{ph} + E^0(O_2/H_2O) \quad (1)$$

On the basis of eq 1,  $\eta_k$  decreases about 150 mV, displaying that the negative shift of  $V_{on}$  after NiFe-LDH deposition is mainly due to the kinetic factor. It is further supported by electrochemical active surface area (ECSA) measurements and XPS. An increase of ECSA by 4.6-fold (Figure S8b, Supporting Information) after NiFe-LDH deposition, an enhancement of the Ni<sup>3+</sup> signal intensity (XPS Ni 2p, red curve in Figure 4), and introduction of Fe (XPS in Figure S9, Supporting Information) indicate more catalytically active sites are produced, thereby favoring the kinetic reaction.<sup>21,45–49</sup> For the whole  $n^+p$ -Si/SiO<sub>x</sub>/Ni/NiO<sub>x</sub>/NiFe-LDH photoanode, both energetic and kinetic factors contribute to the excellent performance as quantitatively summarized in Table 1.

**Table 1. Summary of Water Oxidation Data<sup>a</sup>**

photoanodes	$V_{on}$ (V*) <sup>a</sup>	$V_{@10}^b$ (V*)	$V_{ph}$ (V)	$V_{fb}$ (V*)	$\eta_k$ (V)
Ni/NiO <sub>x</sub> /NiFe-LDH	0.78	0.91	0.608	−0.102	0.158
Ni/NiO <sub>x</sub>	0.96	1.09	0.578	−0.067	0.308
difference	−0.18	−0.18	0.030	−0.035	−0.150

<sup>a</sup>These data values were extracted from Figure 3, where superscript letters *a* and *b* denote the potential versus RHE and the potential corresponding to the photocurrent density of 10 mA cm<sup>-2</sup>, respectively. Ni/NiO<sub>x</sub>/NiFe-LDH and Ni/NiO<sub>x</sub> represent  $n^+p$ -Si/SiO<sub>x</sub>/Ni/NiO<sub>x</sub>/NiFe-LDH and  $n^+p$ -Si/SiO<sub>x</sub>/Ni/NiO<sub>x</sub> photoanodes, respectively.

In this work, the partially activated Ni bridging layer plays an indispensable role in the efficient and stable photoanode integration. Without activation of the Ni layer, an additional potential of  $\sim 70$  mV should be applied in  $n^+p$ -Si/SiO<sub>x</sub>/Ni/NiFe-LDH to reach the current density of 10 mA cm<sup>-2</sup> compared to that in  $n^+p$ -Si/SiO<sub>x</sub>/Ni/NiO<sub>x</sub>/NiFe-LDH (Figure 5a). Electrochemical impedance spectroscopy (EIS) analysis

was carried out to elucidate the effect of NiO<sub>x</sub> on the interfacial charge transport behavior in the photoanodes. The Nyquist plots showing two semicircles at the high-frequency and low-frequency regions, together with the equivalent circuit model (Figure 5b), correspond to charger transfer resistances at the photoanode/electrolyte interface and in the photoanode, respectively.<sup>7,24,50</sup> For  $n^+p$ -Si/SiO<sub>x</sub>/Ni/NiO<sub>x</sub>/NiFe-LDH, both of the semicircle radii were smaller than those of  $n^+p$ -Si/SiO<sub>x</sub>/Ni/NiFe-LDH, indicating the smaller charge transfer resistance at the photoanode/electrolyte interface and in the photoanode. These results demonstrate that NiO<sub>x</sub> greatly improves the OER performance by facilitating transfer of charge carriers both at the photoanode/electrolyte interface and in the bulk photoanode. In addition, severe peeling of NiFe-LDH from the  $n^+p$ -Si/SiO<sub>x</sub>/Ni/NiFe-LDH photoanode occurs after the first CV sweep (Figure S10a,b, Supporting Information). It can be inferred that the dense Ni surface is oxidized to form the porous NiO<sub>x</sub> by the electrolyte penetrating through NiFe-LDH. The consequent volume expansion of NiO<sub>x</sub> between Ni and NiFe-LDH causes exfoliation of NiFe-LDH. The great strain arising from this rapid volume expansion of NiO<sub>x</sub> at the Ni/NiFe-LDH interface causes exfoliation of NiFe-LDH. For the  $n^+p$ -Si/SiO<sub>x</sub>/Ni/NiO<sub>x</sub>/NiFe-LDH anode, a particle-like layer is formed on the Ni surface after activation before NiFe-LDH deposition (Figure 2c, and Figure S3c in Supporting Information), and oxidation of Ni will not go further than  $\sim 2.5$  nm in this layer.<sup>29</sup> NiO<sub>x</sub> (including Ni(OH)<sub>2</sub> and NiOOH) and NiFe-LDH have stronger interfacial interaction such as hydrogen bonding owing to the similar metal hydroxide structure and composition compared to Ni and NiFe-LDH, and the volume of NiO<sub>x</sub> will not further expand after activation, so the high stability is achieved in  $n^+p$ -Si/SiO<sub>x</sub>/Ni/NiO<sub>x</sub>/NiFe-LDH. NiO<sub>x</sub> has a high capacity of hole accumulation<sup>51</sup> and strong bonding with NiFe-LDH, facilitating transfer of accumulated holes to the catalyst. For the  $n^+p$ -Si/SiO<sub>x</sub>/NiFe-LDH photoanode without any Ni-based interlayer, it is difficult to deposit a homogeneous NiFe-LDH film on the Si surface owing to the great difference in material structure and composition between Si and NiFe-LDH (Figure S10c, Supporting Information). Also, the anode performance is really poor with an onset potential of  $\sim 0.950$  V versus RHE and a very low current density of  $\sim 4.7$  mA cm<sup>-2</sup> at 1.23 V versus RHE (Figure S10d, Supporting Information). This comparison of the performance with and without the partially activated Ni bridging layer highlights the importance of the interfacial engineering on the PEC performance improvement. Without proper design of the interface, it is difficult to integrate Si with NiFe-LDH and take full advantage of the merits of each component.

In summary, the  $n^+p$ -Si photoabsorber has been successfully integrated with the NiFe-LDH nanosheet array catalyst by facilely engineering a partially activated Ni bridging layer for a high-efficient, stable, and earth-abundant photoanode. In the  $n^+p$ -Si/SiO<sub>x</sub>/Ni/NiO<sub>x</sub>/NiFe-LDH photoanode, Ni has good contact with Si and protects Si against corrosion, and the NiO<sub>x</sub> layer developed from PEC activation of Ni before NiFe-LDH deposition has strong bonding with NiFe-LDH owing to the similarity in material structure and composition and also avoids exfoliation of NiFe-LDH from the Ni surface caused by the great strain arising from the rapid volume expansion of in-situ growth of NiO<sub>x</sub>. The intimate contact at each interface guarantees smooth charge transfer in the anode and affords the best OER activity and good stability combining with the

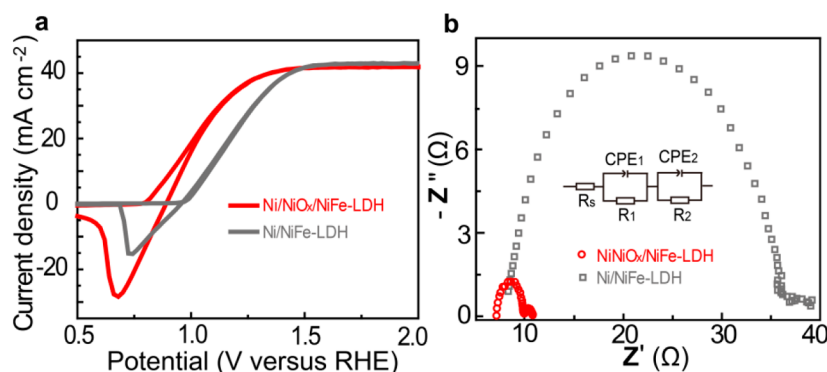


**Figure 5.** PEC performance and electrochemical impedance spectra comparison of photoanodes with and without  $\text{NiO}_x$ . (a) Recorded CV curves of  $\text{Ni/NiO}_x/\text{NiFe-LDH}$  and  $\text{Ni/NiFe-LDH}$  coated  $n^+p\text{-Si/SiO}_x$  photoanodes. (b) Nyquist plots and equivalent circuit model corresponding to the photoanodes in (a).  $\text{CPE}_1$  and  $\text{CPE}_2$  represent constant phase elements,  $R_s$  represents the resistance including series and solution resistances, while  $R_1$  and  $R_2$  represent the charge transfer resistance at the photoanode/electrolyte interface and in the bulk photoanode, respectively.

excellent properties of  $n^+p\text{-Si}$  and  $\text{NiFe-LDH}$  compared to all previous reported crystalline Si-based photoanodes. Our work provides a new, simple, and low-cost interfacial engineering strategy to integrate Si with catalysts to minimize losses and resist degradation and also sheds light on a complete understanding and control of the heterogeneous interface between the photoabsorber and the charge-carrier collector, a crucial aspect of any device structure in the field of solar energy conversion.

## ■ ASSOCIATED CONTENT

### Supporting Information

The Supporting Information is available free of charge on the ACS Publications website at DOI: 10.1021/acs.nanolett.7b05314.

Experiment details, materials and chemicals, electrochemical measurements, Faradaic efficiency, applied bias photon-to-current efficiency, electrochemical active surface area, Mott–Schottky analysis, electrochemical impedance spectroscopy, photovoltage test, analysis of factors in influencing the photocurrent onset potential, PEC device schematic and wiring schematic, CV curves for photoanodes optimization, characterizations of HRTEM, SEM, XRD, XPS, chronoamperometry test, and digital images (PDF)

## ■ AUTHOR INFORMATION

### Corresponding Author

\*E-mail: gongjr@nanoctr.cn.

### ORCID

Jian Ru Gong: 0000-0003-1512-4762

### Author Contributions

B.G. and A.B. contributed equally. All authors have given approval to the final version of the manuscript.

### Notes

The authors declare no competing financial interest.

## ■ ACKNOWLEDGMENTS

The authors acknowledge financial support for this work from the National Natural Science Foundation of China (21422303, 21573049), National Key R&D Program “Nanotechnology” special focus (2016YFA0201600), Beijing Natural Science Foundation (2142036), the Knowledge Innovation Program

and Youth Innovation Promotion Association, Special Program of “One Belt One Road” of CAS, and “CAS-TWAS President’s fellowship”.

## ■ REFERENCES

- (1) Walter, M. G.; Warren, E. L.; McKone, J. R.; Boettcher, S. W.; Mi, Q.; Santori, E. A.; Lewis, N. S. *Chem. Rev.* **2010**, *110*, 6446–6473.
- (2) Montoya, J. H.; Seitz, L. C.; Chakthranont, P.; Vojvodica, A.; Jaramillo, T. F.; Nørskov, J. K. *Nat. Mater.* **2017**, *16*, 70–81.
- (3) Zhang, K.; Dong, T.; Xie, G. C.; Guan, L. M.; Guo, B. D.; Xiang, Q.; Dai, Y. W.; Tian, L. Q.; Batool, A.; Jan, S. U.; Boddula, R.; Thebo, A. A.; Gong, J. R. *ACS Appl. Mater. Interfaces* **2017**, *9*, 42723–42733.
- (4) Fujishima, A.; Honda, K. *Nature* **1972**, *238*, 37–38.
- (5) Tachibana, Y.; Vayssieres, L.; Durrant, J. R. *Nat. Photonics* **2012**, *6*, 511–518.
- (6) Sun, K.; Shen, S.; Liang, Y.; Burrows, P. E.; Mao, S. S.; Wang, D. *Chem. Rev.* **2014**, *114*, 8662–8719.
- (7) Bai, S.; Jiang, J.; Zhang, Q.; Xiong, Y. *Chem. Soc. Rev.* **2015**, *44*, 2893–2939.
- (8) Yang, J.; Wang, D.; Han, H.; Li, C. *Acc. Chem. Res.* **2013**, *46*, 1900–1909.
- (9) Weber, M. F.; Dignam, M. J. *Int. J. Hydrogen Energy* **1986**, *11*, 225–232.
- (10) Yoshikawa, K.; Kawasaki, H.; Yoshida, W.; Irie, T.; Konishi, K.; Nakano, K.; Uto, T.; Adachi, D.; Kanematsu, M.; Uzu, H.; Yamamoto, K. *Nat. Energy* **2017**, *2*, 17032.
- (11) Bae, D.; Pedersen, T.; Seger, B.; Malizia, M.; Kuznetsov, A.; Hansen, O.; Chorkendorff, I.; Vesborg, P. C. K. *Energy Environ. Sci.* **2015**, *8*, 650–660.
- (12) Hou, Y.; Abrams, B. L.; Vesborg, P. C. K.; Björketun, M. E.; Herbst, K.; Bech, L.; Setti, A. M.; Damsgaard, C. D.; Pedersen, T.; Hansen, O.; Rossmeisl, J.; Dahl, S.; Nørskov, J. K.; Chorkendorff, I. *Nat. Mater.* **2011**, *10*, 434–438.
- (13) Cabán-Acevedo, M.; Stone, M. L.; Schmidt, J. R.; Thomas, J. G.; Ding, Q.; Chang, H.-C.; Tsai, M.-L.; He, J.-H.; Jin, S. *Nat. Mater.* **2015**, *14*, 1245–1251.
- (14) Kelzenberg, M. D.; Boettcher, S. W.; Petykiewicz, J. A.; Turner-Evans, D. B.; Putnam, M. C.; Warren, E. L.; Spurgeon, J. M.; Briggs, R. M.; Lewis, N. S.; Atwater, H. A. *Nat. Mater.* **2010**, *9*, 239–244.
- (15) Esposito, D. V.; Levin, I.; Moffat, T. P.; Talin, A. A. *Nat. Mater.* **2013**, *12*, 562–568.
- (16) Heller, A.; Lewerenz, H. J.; Miller, B. J. *Am. Chem. Soc.* **1981**, *103*, 200–201.
- (17) Ji, L.; McDaniel, M. D.; Wang, S.; Posadas, A. B.; Li, X.; Huang, H.; Lee, J. C.; Demkov, A. A.; Bard, A. J.; Ekerdt, J. G.; Yu, E. T. *Nat. Nanotechnol.* **2015**, *10*, 84–90.
- (18) Ji, L.; Hsu, H.-Y.; Li, X.; Huang, K.; Zhang, Y.; Lee, J. C.; Bard, A. J.; Yu, E. T. *Nat. Mater.* **2017**, *16*, 127–131.

- (19) Zhou, X.; Liu, R.; Sun, K.; Papadantonakis, K. M.; Bruntschwig, B. S.; Lewis, N. S. *Energy Environ. Sci.* **2016**, *9*, 892–897.
- (20) Mei, B.; Seger, B.; Pedersen, T.; Malizia, M.; Hansen, O.; Chorkendorff, I.; Vesborg, P. C. K. *J. Phys. Chem. Lett.* **2014**, *5*, 1948–1952.
- (21) Kenney, M. J.; Gong, M.; Li, Y.; Wu, J. Z.; Feng, J.; Lanza, M.; Dai, H. *Science* **2013**, *342*, 836–840.
- (22) Hill, J. C.; Landers, A. T.; Switzer, J. A. *Nat. Mater.* **2015**, *14*, 1150–1155.
- (23) Yang, J.; Cooper, J. K.; Toma, F. M.; Walczak, K. A.; Favaro, M.; Beeman, J. W.; Hess, L. H.; Wang, C.; Zhu, C.; Gul, S.; Yano, J.; Kisielowski, C.; Schwartzberg, A.; Sharp, I. D. *Nat. Mater.* **2017**, *16*, 335–341.
- (24) Yu, X.; Yang, P.; Chen, S.; Zhang, M.; Shi, G. *Adv. Energy Mater.* **2017**, *7*, 1601805.
- (25) Sun, K.; McDowell, M. T.; Nielander, A. C.; Hu, S.; Shaner, M. R.; Yang, F.; Bruntschwig, B. S.; Lewis, N. S. *J. Phys. Chem. Lett.* **2015**, *6*, 592–598.
- (26) Chen, Y. W.; Prange, J. D.; Dühnen, S.; Park, Y.; Gunji, M.; Chidsey, C. E. D.; McIntyre, P. C. *Nat. Mater.* **2011**, *10*, 539–544.
- (27) Sun, K.; Saadi, F. H.; Lichterman, M. F.; Hale, W. G.; Wang, H.-P.; Zhou, X.; Plymale, N. T.; Omelchenko, S. T.; He, J.-H.; Papadantonakis, K. M.; Bruntschwig, B. S.; Lewis, N. S. *Proc. Natl. Acad. Sci. U. S. A.* **2015**, *112*, 201423034.
- (28) Reece, S. Y.; Hamel, J. A.; Sung, K.; Jarvi, T. D.; Esswein, A. J.; Pijpers, J. J. H.; Nocera, D. G. *Science* **2011**, *334*, 645–648.
- (29) Digdaya, I. A.; Adhyaksa, G. W. P.; Trześniewski, B. J.; Garnett, E. C.; Smith, W. A. *Nat. Commun.* **2017**, *8*, 15968.
- (30) Yao, T.; Chen, R.; Li, J.; Han, J.; Qin, W.; Wang, H.; Shi, J.; Fan, F.; Li, C. *J. Am. Chem. Soc.* **2016**, *138*, 13664–13672.
- (31) Scheuermann, A. G.; Lawrence, J. P.; Kemp, K. W.; Ito, T.; Walsh, A.; Chidsey, C. E. D.; Hurley, P. K.; McIntyre, P. C. *Nat. Mater.* **2016**, *15*, 99–105.
- (32) Chen, L.; Yang, J.; Klaus, S.; Lee, J.; Woods-Robinson, R.; Ma, J.; Lum, Y.; Cooper, J. K.; Toma, F. M.; Wang, L.-W.; Sharp, I. D.; Bell, A. T.; Ager, J. W. *J. Am. Chem. Soc.* **2015**, *137*, 9595–9603.
- (33) Sun, K.; Shen, S.; Cheung, J. S.; Pang, X.; Park, N.; Zhou, J.; Hu, Y.; Sun, Z.; Noh, S. Y.; Riley, C. T.; Yu, P. K. L.; Jin, S.; Wang, D. *Phys. Chem. Chem. Phys.* **2014**, *16*, 4612–4625.
- (34) Hu, S.; Shaner, M. R.; Beardslee, J. A.; Lichterman, M.; Bruntschwig, B. S.; Lewis, N. S. *Science* **2014**, *344*, 1005–1009.
- (35) Cox, C. R.; Winkler, M. T.; Pijpers, J. J. H.; Buonassisi, T.; Nocera, D. G. *Energy Environ. Sci.* **2013**, *6*, 532–538.
- (36) Qi, X.; She, G.; Huang, X.; Zhang, T.; Wang, H.; Mu, L.; Shi, W. *Nanoscale* **2014**, *6*, 3182–3189.
- (37) Lin, F.; Boettcher, S. W. *Nat. Mater.* **2014**, *13*, 81–86.
- (38) Gong, M.; Dai, H. *Nano Res.* **2015**, *8*, 23–39.
- (39) Ning, F.; Shao, M.; Xu, S.; Fu, Y.; Zhang, R.; Wei, M.; Evans, D. G.; Duan, X. *Energy Environ. Sci.* **2016**, *9*, 2633.
- (40) LeRoy, R. L. *Int. J. Hydrogen Energy* **1983**, *8*, 401–417.
- (41) Gong, J. R. *Small* **2010**, *6*, 967–973.
- (42) Yoshikawa, K.; Kawasaki, H.; Yoshida, W.; Irie, T.; Konishi, K.; Nakano, K.; Uto, T.; Adachi, D.; Kanematsu, M.; Uzu, H.; Yamamoto, K. *Nat. Energy* **2017**, *2*, 17032.
- (43) Trotochaud, L.; Ranney, J. K.; Williams, K. N.; Boettcher, S. W. *J. Am. Chem. Soc.* **2012**, *134*, 17253–17261.
- (44) Gorlin, Y.; Jaramillo, T. F. *J. Am. Chem. Soc.* **2010**, *132*, 13612–13614.
- (45) Malara, F.; Fabbri, F.; Marelli, M.; Naldoni, A. *ACS Catal.* **2016**, *6*, 3619–3628.
- (46) Mei, B.; Permyakova, A. A.; Frydendal, R.; Bae, D.; Pedersen, T.; Malacrida, P.; Hansen, O.; Stephens, I. E. L.; Vesborg, P. C. K.; Seger, B.; Chorkendorff, I. *J. Phys. Chem. Lett.* **2014**, *5*, 3456–3461.
- (47) Zhu, X.; Tang, C.; Wang, H.-F.; Zhang, Q.; Yang, C.; Wei, F. *J. Mater. Chem. A* **2015**, *3*, 24540–24546.
- (48) Li, Z.; Shao, M.; An, H.; Wang, Z.; Xu, S.; Wei, M.; Evans, D. G.; Duan, X. *Chem. Sci.* **2015**, *6*, 6624–6631.
- (49) Xiao, C.; Li, Y.; Lu, X.; Zhao, C. *Adv. Funct. Mater.* **2016**, *26*, 3515–3523.
- (50) Zhang, H.; Ding, Q.; He, D.; Liu, H.; Liu, W.; Li, Z.; Yang, B.; Zhang, X.; Lei, L.; Jin, S. *Energy Environ. Sci.* **2016**, *9*, 3113–3119.
- (51) Cui, C.; Heggen, M.; Zabka, W. D.; Cui, W.; Osterwalder, J.; Probst, B.; Alberto, R. *Nat. Commun.* **2017**, *8*, 1341.